energies

MDPI

Article

Spectrum-Dependent Burnable Poison Selection for Enhanced Safety and Neutronic Performance in an Epithermal Supercritical Carbon Dioxide-Cooled Reactor

Yiming Zhong [1], Jing Wen [1], Wenbin Wu [1,*], Naibin Jiang [1], Xiaoqi Zhou [1], Di Lu [2], Bin Zhang [2] and Lianjie Wang [2]

[1] Sino-French Institute of Nuclear Engineering and Technology, Sun Yat-Sen University, Zhuhai 519082, China; zhongym29@mail.sysu.edu.cn (Y.Z.)
[2] Science and Technology on Reactor System Design Technology Laboratory, Nuclear Power Institute of China, Chengdu 610041, China
* Correspondence: wuwb28@mail.sysu.edu.cn

Abstract

This study investigates the neutronic performance of burnable poisons (BPs) in an epithermal spectrum supercritical carbon dioxide (S-CO_2)-cooled reactor. Twelve candidate BP materials are systematically evaluated, including rare-earth oxides (e.g., HfO_2, Er_2O_3, Eu_2O_3, etc.) and boron-based compounds (B_4C and PACS). The deterministic neutron transport code KYLIN-I with the ENDF/B VI 45-group cross-section library is employed for analysis. According to the calculation results, Eu_2O_3 effectively suppresses the initial k_{inf} of the epithermal-spectrum fuel assembly to ~1.2 with a relatively low weight fraction (~2.6%) while maintaining a total temperature coefficient (TTC) lower than −1.4 pcm/K throughout the entire burnup period. HfO_2 and Er_2O_3, at approximately 15% weight fraction, achieve TTC values better than −2 pcm/K. Furthermore, both Eu_2O_3 and HfO_2 contribute to maintaining a low, stable power peaking factor (PPF) below 1.24 throughout the burnup process. This study provides a theoretical foundation and technical support for designing an efficient and safe S–CO_2-cooled nuclear reactor. It highlights the importance of selecting BP materials that are well-adapted to the neutron spectrum and optimizing the fuel assembly configuration accordingly.

Keywords: burnable poisons; S–CO_2-cooled reactor; KYLIN-I; neutronic performance

1. Introduction

Advanced gas-cooled reactor (AGR) technology has been widely developed worldwide. Currently, the gas-cooled reactor designs generally employ the helium Brayton cycle system. Examples include the high-temperature gas-cooled pebble-bed reactor (HTGR) in China [1] and the high-temperature engineering test reactor (HTTR) in Japan [2]. The helium Brayton cycle can achieve core outlet temperatures exceeding 850 °C. However, it imposes stringent requirements on high-temperature-resistant structural materials [3]. Another promising coolant for gas-cooled reactors is S–CO_2 [4,5]. The critical point of CO_2 occurs at a pressure of 7.38 MPa and a temperature of 31.1 °C. S–CO_2 exhibits high thermodynamic efficiency within the temperature range of 450–600 °C, making it well-suited for nuclear energy applications [6]. Other outstanding properties, such as high density, low viscosity, and compact turbomachinery, further improve its potential.

Check for updates

Academic Editor: Sung Joong Kim

Received: 29 November 2025
Revised: 23 December 2025
Accepted: 29 December 2025
Published: 30 December 2025

Copyright: © 2025 by the authors. Licensee MDPI, Basel, Switzerland. This article is an open access article distributed under the terms and conditions of the Creative Commons Attribution (CC BY) license.

In the 2000s, research institutions in the United States, such as the Massachusetts Institute of Technology (MIT) [7–9] and Sandia National Laboratories (SNL) [10] published a series of studies exploring both direct and indirect applications of the S–CO_2 Brayton cycle in nuclear engineering. The innovative reactor design concept, which utilizes S–CO_2 as a direct coolant, has the potential to further enhance economic performance and simplify system configuration [11,12]. Building on this advantage, several studies have proposed the S–CO_2-cooled reactor as a transportable micro-reactor [13–15].

Unlike light water, S–CO_2 coolant has inherent limitations in neutron moderation and weak temperature reactivity feedback. Researchers have proposed installing moderator rods into the S–CO_2 gas-cooled reactor's fuel assembly to enhance the neutron moderation. Due to the nature of AGR, only solid moderators are suitable for the S–CO_2 reactor core. By comparing different moderator materials and their configurations, an optimized design for an S–CO_2 gas-cooled reactor fuel assembly was developed, also known as a "weak moderation" assembly [16,17]. Meanwhile, the solid moderator shifts the neutron energy spectrum from fast to the epithermal energy range [18].

Besides reactivity feedback mechanisms, the auxiliary reactivity control methods are essential for ensuring the safety of S–CO_2 reactor cores, such as the burnable poison (BP) reactivity control method [19]. Compared with control rod mechanisms, BPs offer greater flexibility, as they can be integrated into fuel assemblies without requiring additional space for facility configurations [20,21]. The application of BPs for reactivity control has been extensively investigated across various advanced reactor types. These include rectangular and plate-shaped assembly water-cooled small modular reactors (SMRs) [22–25], liquid metal-cooled fast-spectrum nuclear reactors (LMCRs) [26,27], and high-temperature gas-cooled reactors (HTGRs). For HTGRs, the feasibility of using BPs has been well studied under both thermal and fast neutron spectra [28,29]. Additionally, BP design concepts are also applicable to micro-transportable gas-cooled reactors that have a similar design to the S–CO_2-cooled reactor [30,31]. Theoretically, the BP-based reactivity control method applies to any nuclear reactor.

BP materials control reactivity by interacting with neutrons through absorption reactions such as (n, γ), (n, α), and (n, p). Core design characteristics significantly influence the practical performance of BP design. Variations in the neutron spectrum have a significant effect on reactor core features. Previously, Hwanyeal Yu [32] studied 90% enriched ^{10}B B_4C or Hf as a "replaceable fixed absorber (RFA)" in a 36.2 WM_{th} S-CO_2-cooled micro modular reactor (MMR). Zhang et al. [33] also employed B_4C in discrete BP rods in a 15 MW_{th} S–CO_2-cooled microreactor to control radial power distribution. Zong's paper [34] presents the effects of B_4C, Er_2O_3, and Gd_2O_3 on the reactivity disturbance characteristics of the S–CO_2 reactor.

This work focuses on weakly moderated S–CO_2 reactor assemblies, where the neutron absorption cross-sections of candidate isotopes exhibit overlapping resonance peaks in the epithermal energy range. To address this challenge, this study employs the neutronics simulation code KYLIN-I to model epithermal S–CO_2 fuel assemblies and evaluate the performance of a series of BP materials. The numerical simulations are designed to isolate the effect of the epithermal neutron spectrum on BP performance by minimizing the influence of other variables in the neutronic analysis.

The objective of this study is to identify a suitable BP material for the "weak moderation" epithermal-spectrum S–CO_2-cooled reactor and to evaluate its effect on neutronic performance. This paper is organized as follows. Section 2 introduces the candidate BP materials for epithermal reactors and provides an overview of the simulation framework. Section 3 presents the BP performance results for S–CO_2 fuel assemblies. The evaluation metrics include reactivity suppression, temperature feedback behavior, burnup characteris-

tics, and power distribution flattening, thereby enabling a comprehensive assessment of the design performance.

2. Methodology

2.1. Absorber Material Selection

The neutronic design of BPs in epithermal reactors should follow key principles: (1) At the start of operation, BPs must introduce enough negative reactivity to suppress excess reactivity. (2) During operation, BPs should provide consistent reactivity control, enable uniform fuel burnup, and ensure optimal power distribution within the assembly. (3) At the end of the burnup cycle, the reactivity release caused by BP addition should be minimized [32,33]. To meet these design principles, an ideal BP material should have a high-neutron-absorption cross-section, and its transmutation products in the depletion chain should have significantly lower absorption cross-sections. Additionally, the natural abundances of neutron-absorbing isotopes within the BP material must be considered, as they directly affect reactivity control.

According to the literature review, this study conducts a detailed investigation of various rare earth elements as potential BP materials. The selected candidates include hafnium (Hf) [35], europium (Eu) [36], dysprosium (Dy) [37], cadmium (Cd) [38], erbium (Er) [39], samarium (Sm) [40], lutetium (Lu) [41], and holmium (Ho) [42]. It also examines boron (B) and gadolinium (Gd), two well-established BP materials in pressurized water reactors (PWRs), to provide a basis for comparison with rare earth candidates. Data on the (n, γ) cross-section variations with neutron energy for major rare earth element neutron absorption nuclides have been collected from the ENDF/B-VI data library and summarized in Figure 1. Furthermore, the oxides of these rare earth elements all exhibit high melting points, good thermal conductivity, and minimal radiation-induced swelling, making them well-suited for use as BPs in nuclear reactors.

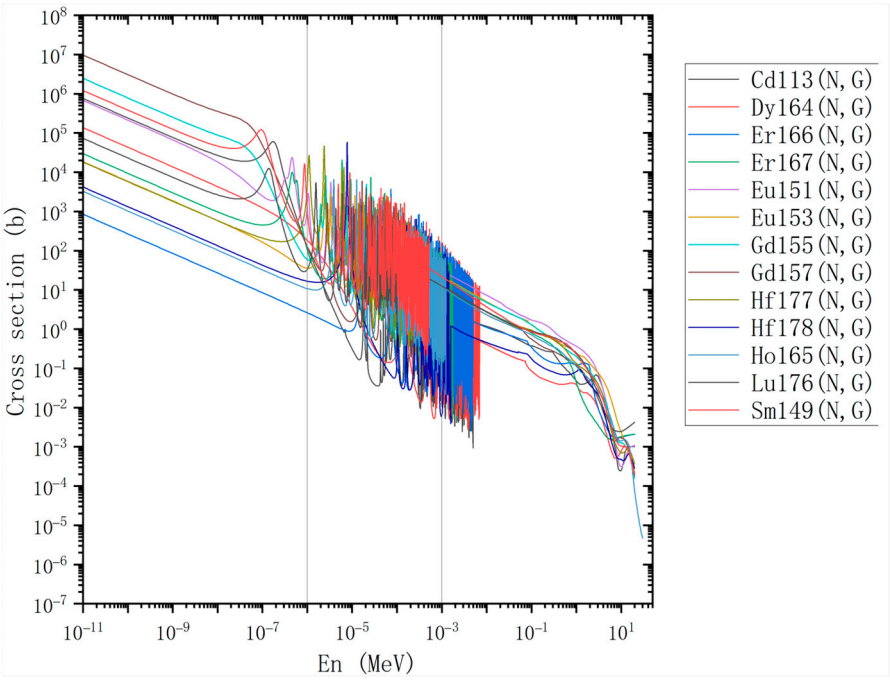


Figure 1. Variation of (n, γ) neutron absorption reaction cross-section with incident neutron energy of major rare earth burnable poison nuclides.

This study also identifies polycarborane-siloxane-ethynyl polymer (PACS), with the molecular formula $(B_{10}H_{10}C_2)_a((CH_3)SiO)_b(C_2)_c$, as a promising BP material. PACS

uniquely combines neutron moderation provided by hydrogen atoms with boron-based neutron absorption [43]. Furthermore, it exhibits excellent thermal stability, enabling it to maintain structural integrity and functionality under high-temperature and high-pressure environments. This study selected two types of PACS materials, PACS-L and PACS-J, with H/B proportions of 84:10 and 34:10 as candidate BP materials. While irradiation stability in polymeric composites has been studied [44,45], direct irradiation data specific to PACS under S–CO_2-cooled radiation conditions remain unavailable. Therefore, this work focuses on evaluating the neutronic performance of PACS materials. Stability concerns under irradiation may be addressed through optimized BP loading methods or compositional adjustments in future work. A set of key parameters for the candidate BP materials selected in this study is summarized in Table 1.

Table 1. The primary material properties parameters of candidate BP materials.

Candidate BP Materials	Primary Neutron Absorber Isotopes	Natural Abundance of Absorbing Nuclides	Density (g/cm^3)	Melting Point (°C)
Gd_2O_3	^{155}Gd	0.1480	7.40	2330
	^{157}Gd	0.1565		
Er_2O_3	^{166}Er	0.3350	8.64	2387
	^{167}Er	0.2287		
Eu_2O_3	^{151}Eu	0.4781	7.30	2350
	^{153}Eu	0.5219		
HfO_2	^{176}Hf	0.0526	9.68	2758
	^{177}Hf	0.1860		
	^{178}Hf	0.2728		
	^{179}Hf	0.1362		
	^{180}Hf	0.3508		
CdO	^{113}Cd	0.1222	8.15	900
Sm_2O_3	^{149}Sm	0.1382	8.35	2325
Ho_2O_3	^{165}Ho	1.0000	8.36	2330
Dy_2O_3	^{164}Dy	0.2826	7.81	2330–2350
Lu_2O_3	^{176}Lu	0.0260	9.42	2487
B_4C	^{10}B	0.1982	2.52	2450
PACS-L	^{10}B		0.9	>1200
PACS-J	^{10}B		1.0	>1200

2.2. Fuel Assembly Configuration

This study incorporates the candidate materials into simulated reactor fuel assemblies and calculates the corresponding neutronic parameters. Their performance is then assessed to identify suitable BP candidates for an epithermal-spectrum S–CO_2-cooled reactor core. To examine how the neutron spectrum affects BP performance, two different fuel assembly models are created: an epithermal-spectrum fuel assembly (ES-FA) representing a mildly moderated S–CO_2-cooled reactor core and a fast-spectrum fuel assembly (FS-FA) without ZrH_2 rods. Both configurations are shown in Figure 2.

The fuel assembly models in this study are based on the published design of a "weak moderation" S–CO_2-cooled reactor. The reactor core has a thermal power of 100 MW_{th}, with S–CO_2 coolant entering the core at 671 K and exiting at approximately 850 K. Each fuel assembly has a hexagonal geometry and consists of 61 rods. The fuel rods are composed of UO_2 with a ^{235}U enrichment of 19.75%, and the cladding material is high-nickel-content stainless steel. In the ES-FA assembly model, 13 ZrH_2 moderator rods are incorporated. The key geometric and material parameters of the fuel assemblies are summarized in Table 2.

The integrated BP rod refers to a configuration in which the BP material is directly incorporated into the nuclear fuel. Fabrication methods include surface coating of fuel pellets or sintering a uniformly mixed BP–UO_2 matrix [46]. Figure 3 shows schematic diagrams of BP-coated and uniformly mixed integrated BP rods. In this study, a heterogeneous neutronic model of the S–CO_2-cooled fuel assembly is used to reflect the spatial

heterogeneity of BP material distribution. Specifically, fuel rods containing a homogenized BP–UO_2 mixture are modeled as separate material cells with unique isotopic compositions and densities, unlike standard UO_2 fuel rods.

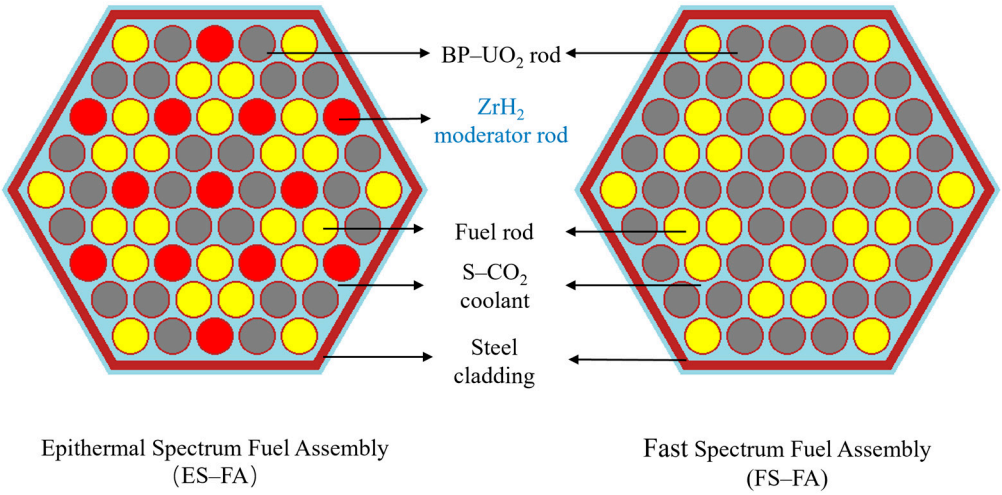


Figure 2. The fuel assembly models in the epithermal and fast neutron spectrums.

Table 2. Benchmark epithermal-spectrum nuclear reactor fuel assembly major parameters.

Design Parameters	Value
Radius of the fuel rod	3.5 mm
Number of rod cells	61
Rod pitch	0.9 cm
Thickness of cladding	0.5 mm
Assembly box thickness	2 cm
Density of UO_2 fuel	10.4 g/cm^3
^{235}U enrichment	19.75%
Supercritical CO_2 coolant density	0.11519 g/cm^3
Temperature of fuel	900 K
Temperature of coolant	773 K
Solid moderator material	ZrH_2

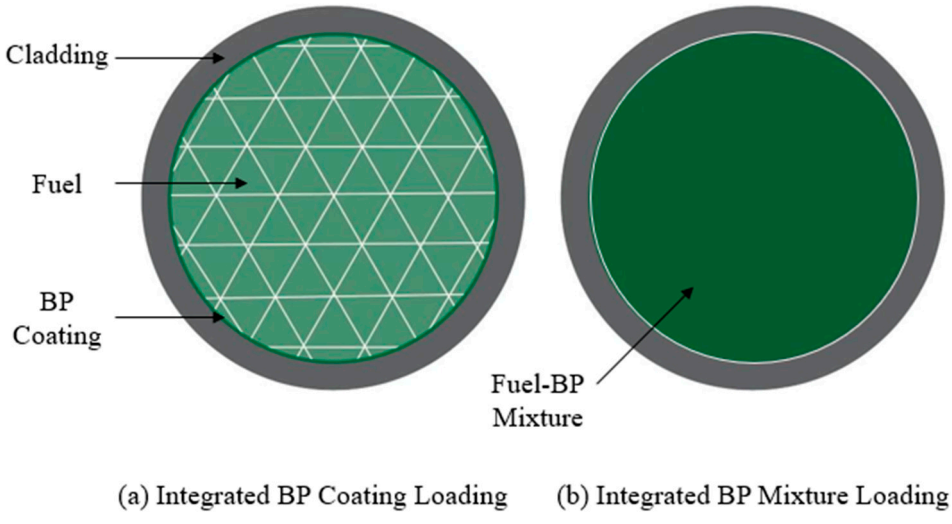


Figure 3. Schematic diagram of different integrated burnable poison loading methods in rod cells. (**a**) diagram for integrated BP coating loading; (**b**) diagram for integrated BP mixture loading.

2.3. KYLIN-I

The KYLIN-I code is used for neutron transport and burnup calculations in this study. It employs a point-and-line approach for geometric modeling, enabling accurate representation of complex geometries through a combination of straight lines and circular arcs. The neutron transport equation is solved using a flow-coupled collision probability method. KYLIN-I uses the subgroup method to account for resonance self-shielding in cross-section calculations. This method is widely applied in recently developed neutronic analysis codes, such as SHARK [47], NECP-X [48], and MPACT [49].

During development, KYLIN-I was verified and validated against IAEA benchmark problems, with results for k_{inf} and key nuclide density changes during burnup matching reference results [50]. A series of sensitivity studies was conducted to determine the optimal conditions for neutronic calculations. Section 3 will present some results.

3. Results and Discussion

3.1. Sensitivity Analysis

3.1.1. Code Benchmark

A benchmark was performed comparing KYLIN-I with the Monte Carlo method (MCM) code OpenMC [51] using the ES-FA model. It should be noted that BP–UO_2 rods were replaced with fuel rods in this benchmark to eliminate the influence of BP materials. As shown in Figure 4, the k_{inf} from KYLIN-I is 423 pcm higher than OpenMC. This study initially employs KYLIN-I to quantify the neutronic characteristics of BP candidates and then uses OpenMC to reassess the impact of code sensitivity on critical design performance. The OpenMC simulations are performed with 300 batches, including 100 inactive batches. Each batch uses 500,000 source neutrons.

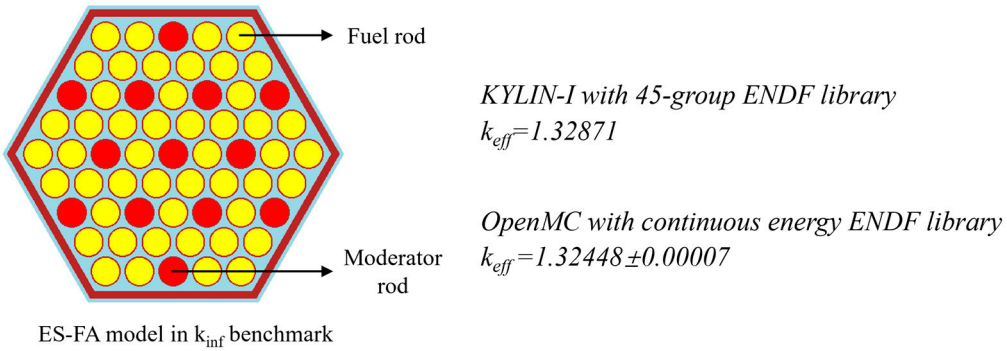


Figure 4. Radial lattice of ES-FA used in benchmark and results from KYLIN-I and OpenMC.

3.1.2. Multi-Group Energy Structure

The KYLIN-I code has been developed and validated using multiple standard multi-group cross-section libraries, including the 45- and 190-group neutron libraries derived from the ENDF/B-VI evaluated nuclear data library. A series of comparisons between these two multigroup neutron libraries was conducted to assess their sensitivity regarding the performance of BP material. Figure 5 shows the k_{inf} results for various ES-FA fuel assemblies with different BP configurations, as calculated by KYLIN-I using both the 45- and 190-group neutron cross-section libraries. For ES-FA cases containing BP materials, the k_{inf} differences between the two libraries generally range from 200 to 500 pcm.

However, the current 190-group neutron library lacks cross-section data for several necessary BP materials, such as Er_2O_3, Eu_2O_3, Gd_2O_3, and HfO_2. To ensure consistency in the neutronic analysis across all BP candidates, subsequent coefficients calculated were performed using the 45-group cross-section library [52]. The outstanding BP cases would be re-evaluated using the OpenMC continuous energy cross-section library.

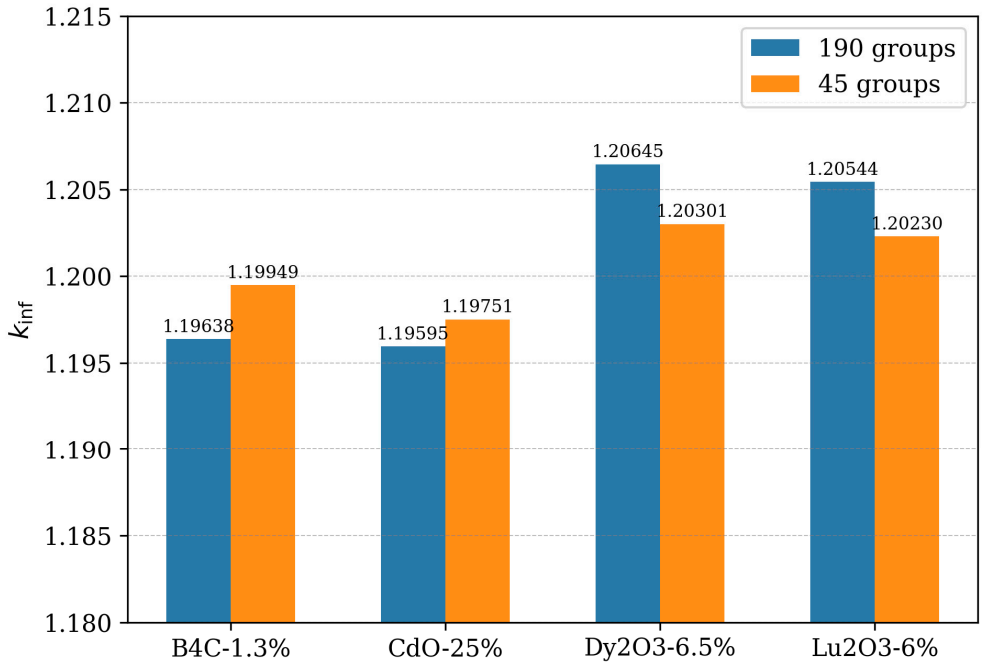


Figure 5. Comparison of k_{inf} values obtained with KYLIN-I using 45 and 190 groups neutron cross-section libraries for various ES-FA BP configurations.

3.1.3. Mesh Subdivision and Burnup

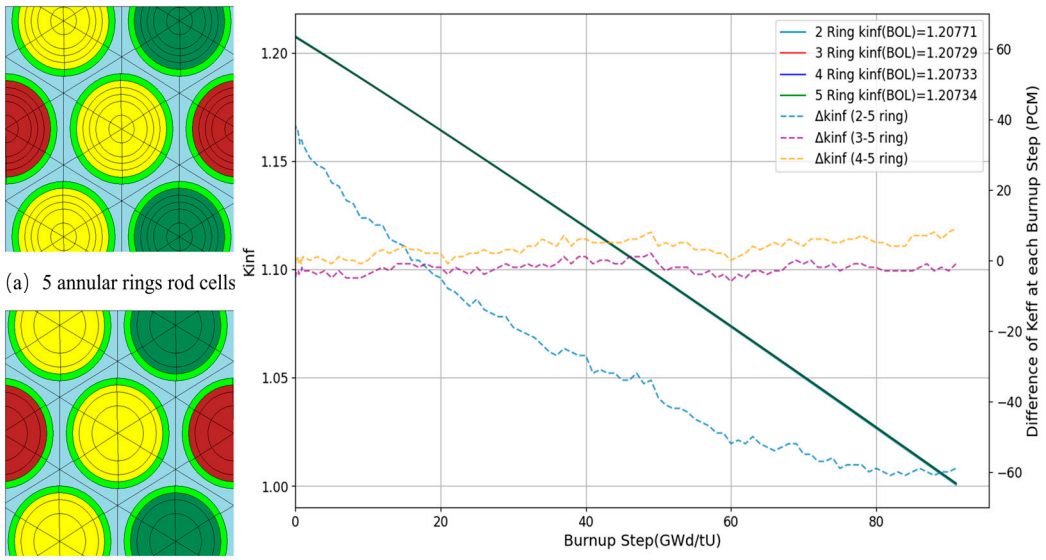
Geometric mesh subdivision has a significant influence on the accuracy of KYLIN-I neutron transport calculations, particularly in BP material performance studies where self-shielding effects are prominent. To evaluate this sensitivity, fuel, and BP pin cells are divided into a varying number of annular rings radially, with each ring assigned homogeneous materials such as UO_2 or BP–UO_2 mixtures.

Burnup calculations evaluated irradiation effects across all mesh configurations. The KYLIN-I code employs a predictor–corrector (PC) scheme for burnup, whereby neutron transport and depletion calculations are performed twice within each burnup step. The nuclide density $\boldsymbol{N}(t)_s$ at step s is computed as shown in Equation (1):

$$\boldsymbol{N}(t)_s = 0.5[exp\,(\boldsymbol{A}_P t)\boldsymbol{N}(0)_s + exp(\boldsymbol{A}_C\, t)\,\boldsymbol{N}(0)_s \quad (1)$$

where $\boldsymbol{A}$ is the transition matrix that incorporates the neutron flux and reaction cross-sections at step s, the subscripts P and C denote the predictor and corrector steps, respectively. $\boldsymbol{N}(0)_s$ represents the nuclide density at the beginning of step s, which serves as the initial composition for both the predictor and corrector. To evaluate mesh sensitivity, a case study was performed simulating 5 wt% Gd_2O_3 in UO_2 fuel at a power density of 25 W/g during burnup. In this sensitivity analysis, the five-ring rod cell case, which has the finest structure, serves as the reference case. Figure 6 shows pin cells with five- and three-ring annular mesh subdivisions, along with the evolution of k_{inf} and its deviation from the reference case during burnup.

The results indicate that while the two-ring pin cell case exhibits significant deviations from the five-ring reference throughout burnup, the three- and four-ring models show much more minor differences, typically within ±10 pcm. In particular, the k_{inf} values for the three-ring case deviate by less than 5 pcm from the reference, demonstrating sufficient accuracy for BP performance analysis. Therefore, a three-ring radial subdivision is adopted in this study to strike a balance between computational efficiency and numerical precision. The entire mesh division used in the corresponding analysis of ES-FA is shown in Figure 7.



(a) 5 annular rings rod cells

(b) 3 annular rings rod cells

(c) k_{inf} and Δk_{inf} versus burnup of several annual ring rod cell subdivision simulation cases

Figure 6. (**a**,**b**): Radial mesh subdivision of the pin cell with five- and three-ring configurations; (**c**): k_{inf} and its deviation from the five-ring reference case as a function of burnup for different mesh subdivisions.

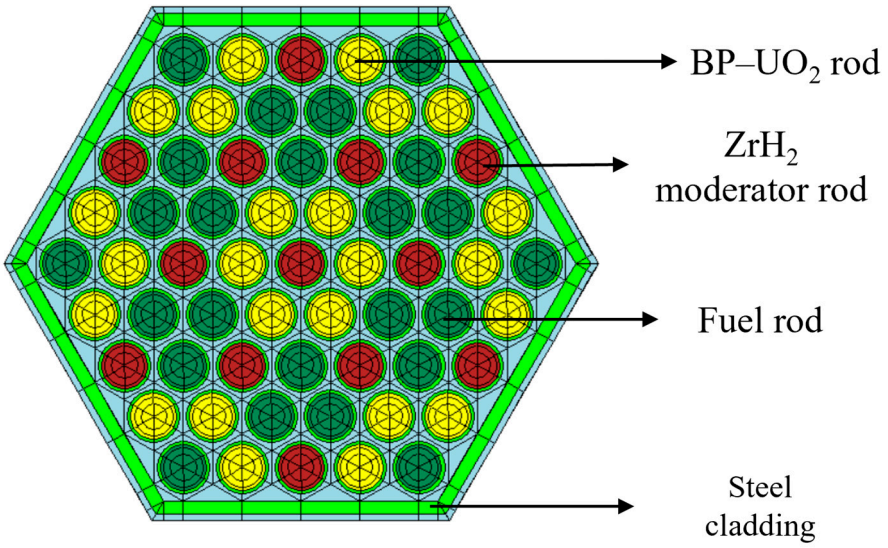


Figure 7. Mesh division of the epithermal-spectrum fuel assembly in the KYLIN-I code.

3.1.4. Initial ^{235}U Content Maintenance

When moderator rods and BP–UO_2 rods are introduced into the S–CO_2-cooled FA model, the effective ^{235}U loading is reduced. To maintain a consistent reactivity benchmark, two compensation strategies are proposed and evaluated in sensitivity analysis, as summarized in Figure 8.

In the "UO_2 material method," a single modified UO_2 material definition, which is adjusted for either ^{235}U enrichment or numerical density (ND), is applied globally in all fuel rods, corresponding to a homogeneous adjustment.

In contrast, the "material cell method" applies separate adjustments to individual material cells. Particularly, standard fuel rods compensate for ^{235}U loss due to moderator volume displacement, while BP–UO_2 rods compensate for loss caused by BP insertion. This yields two distinct UO_2 material definitions, representing a heterogeneous adjustment.

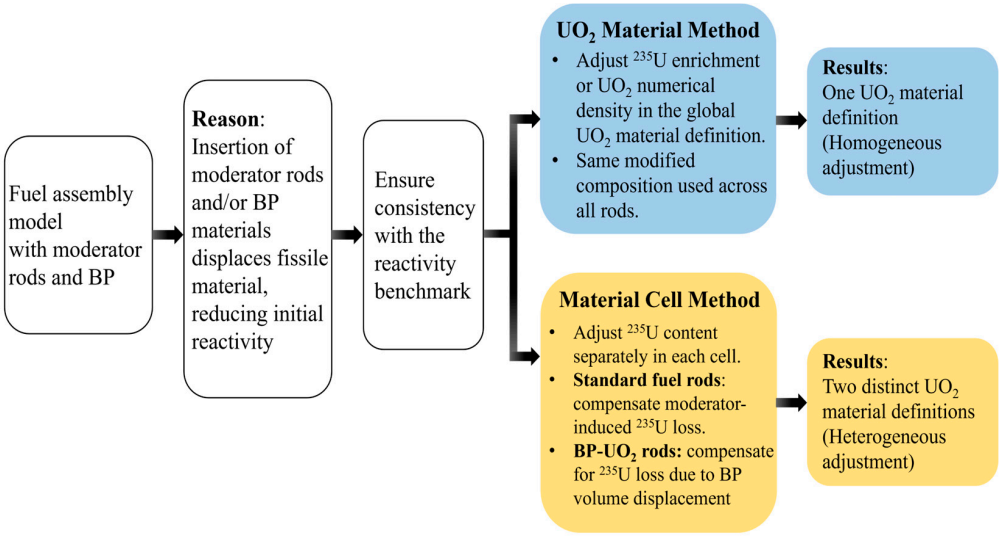


Figure 8. The schematic summary illustrates the ^{235}U compensation logic of the two adjustment strategies.

As shown in Figure 8, the reactivity compensation strategy varies with the assembly configuration. In the ES-FA, both moderator rods and BP–UO_2 rods are incorporated, so the adjustment accounts for the combined loss of ^{235}U due to volume displacement. Conversely, the FS-FA includes only BP–UO_2 rods without moderator rods, meaning the compensation is designed solely to offset the loss of ^{235}U caused by the BP insertion.

The above BP rods with a 5 wt% Gd_2O_3 UO_2 mixture calculation case are used to assess the effectiveness of two compensation strategies under different spectral conditions. The corresponding input parameters are summarized in Table 3. For the "material cell method," parameters are specified separately for UO_2 in standard fuel rods and in BP–UO_2 mixture rods. A reference model, consisting of 61 pure UO_2 fuel rods without moderator rods or BP materials, was also created to examine the inherent burnup behavior of the fast-spectrum S–CO_2-cooled reactor fuel assembly, referred to as the "Only UO_2 fuel assembly" case.

Table 3. Summary of KYLIN-I input parameters for ^{235}U compensation adjustment methods and k_{inf} at the beginning of life (BOL) with various adjustment cases.

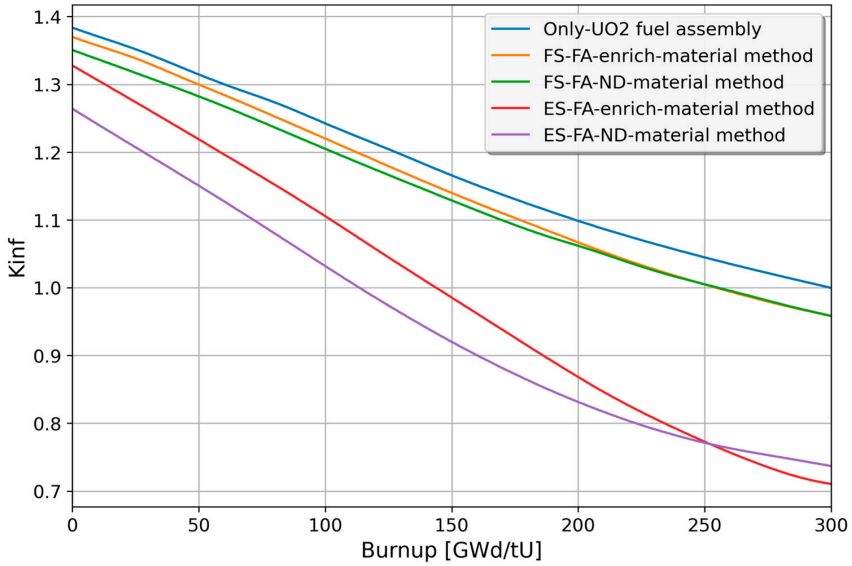
	Assembly Type	Enrichment of ^{235}U	ND (g/cm^3)	Adjusted Enrichment k_{inf} (BOL)	Adjusted ND k_{inf} (BOL)
UO_2 material method	ES-FA	25.997%	13.69	1.32779	1.26405
	FS-FA	20.61%	10.85	1.36988	1.35064
Material cells method (Standard fuel/ BP–UO_2 mixture)	ES-FA	30.37%/21.18%	16.03/11.17	1.32657	1.26265
	FS-FA	19.75%/21.18%	10.4/11.17	1.36910	1.35076
Only UO_2 fuel assembly		19.75%	10.4	1.38359	1.38359

Several burnup calculations were performed using the parameters listed in Table 3. The total burnup depth and step scheme were determined based on the "Only UO_2 fuel assembly" case, in which k_{inf} approaches 1 after 300 GWd/tU. The burnup step scheme consists of 310 steps: the first two are 0.05 GWd/tU, followed by nine steps of 0.1 GWd/tU, and the remaining 299 steps at 1 GWd/tU each. This depth exceeds the typical refueling burnup of PWRs. Such a high burnup level may pose significant challenges to fuel and cladding materials. However, in this conceptual material selection study, this high burnup depth is selected to distinguish differences in BP depletion rates.

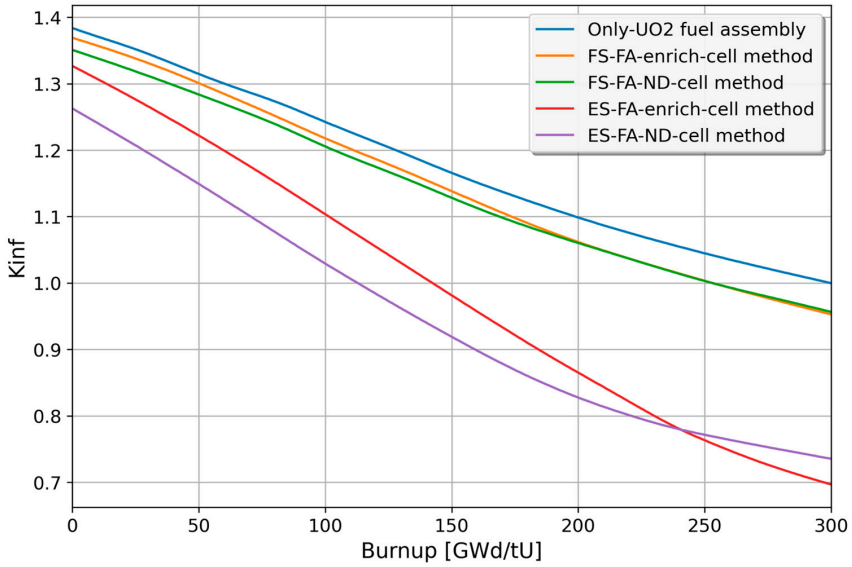
This burnup scheme is consistently applied to all subsequent BP cases throughout this study. The operation condition is simulated at full power, with a power density of 25 W/g. The k_{inf} results at BOL are also shown in Table 3. Compared to the reference "Only UO_2

FA" case, adding Gd_2O_3 BP causes reactivity suppression depending on the spectrum. In FS-FA, the initial k_{inf} decreases from 1.38359 to about 1.370, while in ES-FA, the reduction exceeds approximately 1.327 or 1.264. This significant difference comes from the shift in the neutron spectrum toward the epithermal range caused by the moderator rods, where both ^{238}U resonances and Gd isotopes have notably higher absorption cross-sections.

The depletion curves are shown in Figure 9. The ^{235}U enrichment adjustment leads to higher initial k_{inf} values than the UO_2 ND adjustment under both the material cells method and the UO_2 material method. The reason for this is the decrease in ^{238}U content and lower neutron absorption. Enrichment adjustment also leads to greater Δk_{inf} during burnup. In contrast, the UO_2 ND adjustment maintains the proportion of ^{235}U and ^{238}U, resulting in more stable neutronic performance. The divergence of k_{inf} value between the ^{235}U enrichment and UO_2 ND adjustment methods is more significant in ES-FA assemblies than in FS-FA configurations, as moderator rods amplify the neutron absorption capability of the BP and ^{238}U.



(a) UO_2 material method



(b) Material cells method

Figure 9. The k_{inf} variations in FS-FA and ES-FA with burnup with ^{235}U enrichment and UO_2 ND adjustment methods.

Comparing Figure 9a,b, the UO_2 material method and the material cells method produce similar depletion curves. The material cells method treats the fuel rod parameters independently based on their poison content, offering greater flexibility to model different types of burnable poisons with various weight fractions. Therefore, the material cells method with ND adjustment is selected for subsequent studies to ensure consistency in total fissile material inventory across all computational models.

3.2. Reactivity Suppression

A straightforward opinion about BP design is that increasing the weight fraction (wt%) of BP in the BP–UO_2 mixture rods results in stronger suppression of reactivity. However, the long-term reactivity control is significantly related to the burnup chains of different neutron absorbers. This part of the study chose B_4C and CdO simulation cases to illustrate the impact of the burnup chain. B_4C-type BP materials have a simple neutron reaction as shown in Equation (2).

$$^{10}_{5}B + n = \left[^{11}_{5}B\right]* \rightarrow {}^{7}_{3}Li + {}^{4}_{2}He \quad (2)$$

Another class of candidate BP materials demonstrates long-term reactivity control, such as CdO and HfO_2. When exposed to neutron irradiation, CdO generates isotopes with relatively high-neutron-absorption cross-sections, including ^{107}Ag, ^{109}Ag, and ^{115}In. Figure 10 shows the abundances of Cd isotopes and neutron reaction products.

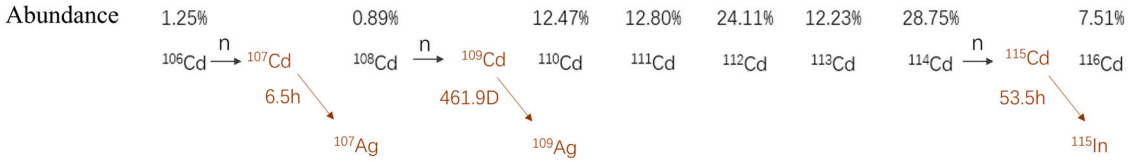


Figure 10. The abundance of Cd isotopes and the high-neutron-absorption cross-section products.

Figure 11 shows the k_{inf} evolutions with burnup of FS-FA and ES-FA assemblies containing different weight fractions of B_4C and CdO poison. The burnup curves for B_4C exhibit significant differences at the initial depletion in both assembly types. However, as burnup progresses, the curves gradually approach each other. Under an epithermal neutron spectrum, the burnup curves of B_4C ES-FA calculation cases collapse into a single line around 150 GWd/tU. Initial differences in reactivity suppression due to varying B_4C weight fraction are minimized by its high depletion rate, which is further enhanced by the inclusion of moderator rods.

Conversely, because of the in situ generation of isotopes with high-neutron-absorption cross-sections, the reactivity suppression effect remains stable throughout the entire burnup process. The burnup curves for different CdO weight fraction cases evolve in parallel, and the assemblies' k_{inf} decreases steadily. Therefore, CdO is better suited as a control rod material rather than a burnable poison.

To further evaluate the BP materials listed in Table 1, a series of calculations was performed to determine the poison weight fractions required to achieve a BOL k_{inf} of 1.200 in both the FS-FA and ES-FA models. The baseline BOL k_{inf} are 1.26265 for ES-FA and 1.35076 for FS-FA. Although the achieved k_{inf} values exhibit slight deviations from the exact target, the corresponding reactivity suppression Δk_{inf} values are precisely quantified for each poison, and their weight fractions are provided in Table 4.

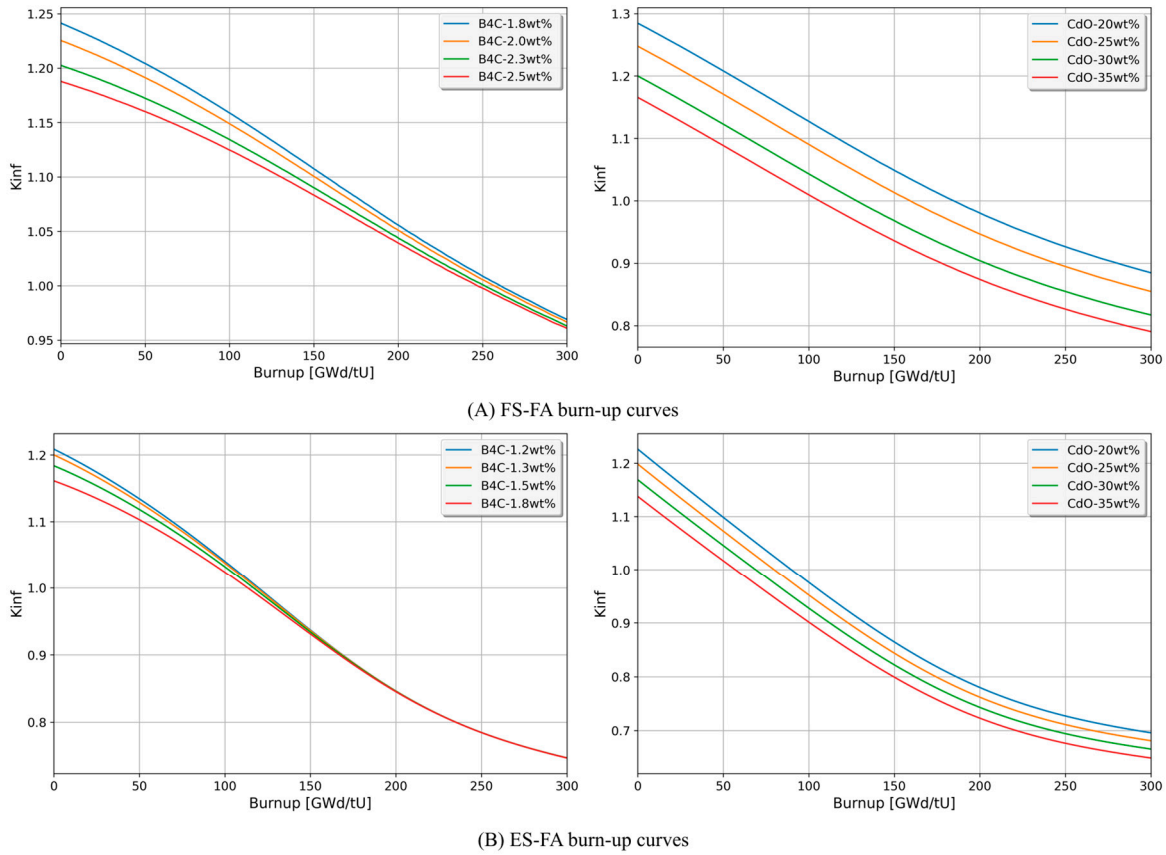


Figure 11. Burnup evolution of k_{inf} in ES-FA and FS-FA models with B_4C and CdO at various weight fractions.

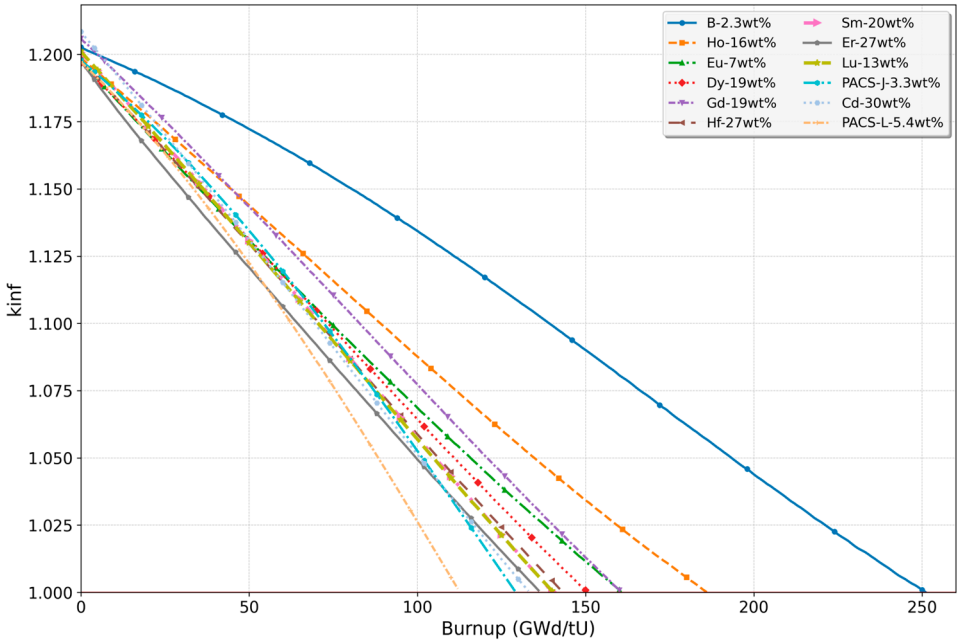
Table 4. Weight fractions of poisonous materials in BP–UO_2 mixture rods for FS-FA and ES-FA models to achieve initial k_{inf} values of 1.2 and burnup depths when k_{inf} values ≈ 1.

	ES-FA			FS-FA		
Poisonous Materials	**Weight Fraction (wt%)**	**BOL Δk_{inf} (pcm)**	**Burnup Depth $k_{inf} \approx 1$ (GWd/tU)**	**Weight Fraction (wt%)**	**BOL Δk_{inf} (pcm)**	**Burnup Depth $k_{inf} \approx 1$ (GWd/tU)**
B_4C	1.3	6230	119	2.3	14,812	258
CdO	25	6404	78	31	14,231	125
Dy_2O_3	6.5	5890	95	19	15,395	153
Er_2O_3	16	6350	83	27	15,306	137
Eu_2O_3	2.6	5874	95	7	15,272	161
Gd_2O_3	10	6301	97	19	14,480	153
HfO_2	15	5960	93	27	15,266	143
Ho_2O_3	8	6677	101	16	15,197	185
Lu_2O_3	6	5952	85	13	14,948	136
Sm_2O_3	7	5838	90	20	15,002	142
PACS-L	5.7	6277	105	5.4	15,283	113
PACS-J	3	6457	109	3.3	15,283	129

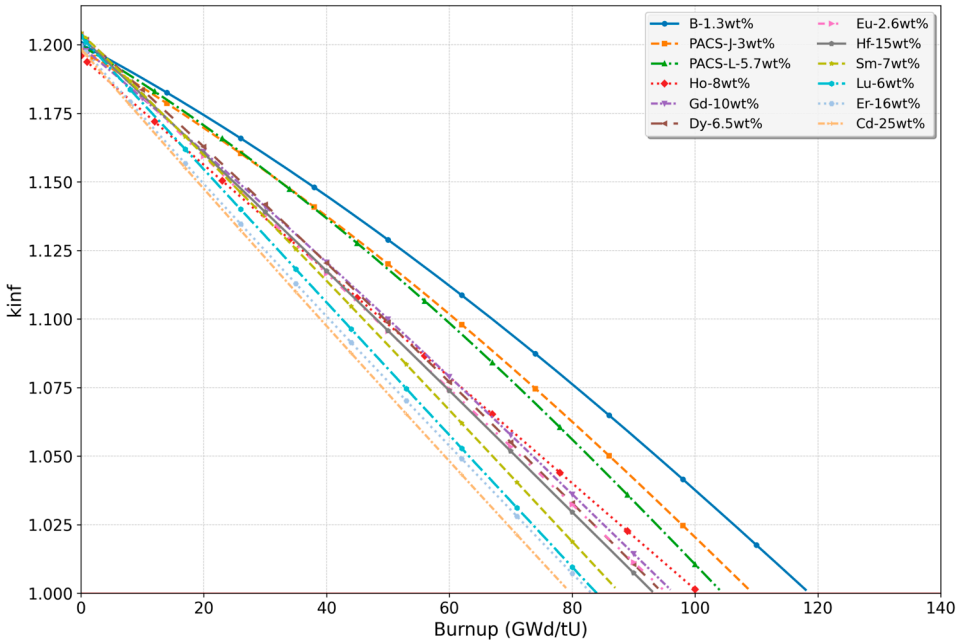
In Table 4, to control the initial k_{inf} of assemblies ~1.2, the weight fractions of poisonous materials in FS-FA assemblies generally range from 10 wt% to 30 wt%. Only the B-based materials have weight fractions below 10 wt%. In ES-FA, except for PACS, the weight fractions of other candidates are about half of those in FS-FA. The addition of moderator rods effectively enhances the initial suppression of reactivity. For B_4C, Dy_2O_3, Eu_2O_3, and Ho_2O_3, these four poisonous materials require much smaller amounts and demonstrate superior reactivity control capabilities under the epithermal spectrum.

Figure 12 presents the burnup curves of FS-FA and ES-FA assemblies with BP material candidates; the initial k_{inf} values are adjusted to approach 1.200 by optimizing weight

fractions as specified in Table 4. The curves are displayed to the point where k_{inf} reaches approximately 1, allowing for a comparative assessment of the FA's depletion rates associated with each BP material. In Figure 12, a general observation is that the ES-FA consistently exhibits a quicker depletion rate and lower weight fractions for all types of BP candidates due to the thermalized neutron spectrum. In the ES-FA, boron-based materials, B_4C and PACS, reach a deeper burnup level when k_{inf} approaches 1 compared to rare-earth element materials. Among the remaining materials, the ES-FA with Ho_2O_3 exhibits a slower k_{inf} decrease rate, followed sequentially by Gd_2O_3, Dy_2O_3, and Eu_2O_3.



(A) FS-FA



(B) ES-FA

Figure 12. The k_{inf} burnup curves of FS-FA/ES-FA with BP candidate, each curve corresponds to a different BP material with adjusted weight fraction in the BP–UO_2 rods.

The loading density of each BP material and the cumulative Δk_{inf} over the entire 300 GWd/tU burnup process are summarized in Table 5. The non-BP reference cases show that the maximum achievable reactivity release for ES-FA is 52,717 pcm, and 39,422 pcm for FS-FA. According to BP optimization principles, an ideal BP should minimize its impact on reactivity release Δk_{inf} while effectively suppressing initial excess reactivity k_{inf} (BOL).

Table 5. The amount of poison loaded in a single BP–UO_2 mixture rod in ES-FA, FS-FA, and Δk_{inf} during 300 GWd/tU.

Poisonous Materials	ES-FA		Poisonous Materials	FS-FA	
	Poison Content (g/cm^2)	300 GWd/tU Δk_{inf} (pcm)		Poison Loading Content (g/cm^2)	300 GWd/tU Δk_{inf} (pcm)
B_4C	0.0126	45,337	B_4C	0.9718	23,966
PACS-J	0.0115	46,952	Ho_2O_3	0.5145	27,501
PACS-L	0.0197	48,959	Eu_2O_3	0.1966	30,612
Ho_2O_3	0.2573	45,054	Dy_2O_3	0.5708	33,185
Gd_2O_3	0.2846	48,429	Gd_2O_3	0.5408	33,319
Dy_2O_3	0.1953	48,233	HfO_2	1.0053	34,551
Eu_2O_3	0.0730	47,020	Sm_2O_3	0.6424	36,907
HfO_2	0.5585	49,318	Er_2O_3	0.8973	35,391
Sm_2O_3	0.2248	51,276	Lu_2O_3	0.4710	36,512
Lu_2O_3	0.2174	52,003	PACS-J	0.0127	40,596
Er_2O_3	0.5317	50,992	CdO	0.9718	38,492
CdO	0.7837	51,762	PACS-L	0.0187	40,596
Non-BP	0	52,717	Non-BP	0	39,422

The reactivity release of FS-FA is apparently lower than that of ES-FA, and the PACS brings a relatively small improvement to the Δk_{inf} over a burnup depth of 300 GWd/tU. In the ES-FA, several rare-earth-based BPs exhibit close Δk_{inf} to the non-BP reference case, which are Lu_2O_3 (52,003 pcm), CdO (51,762 pcm), Sm_2O_3 (51,276 pcm), and Er_2O_3 (50,992 pcm). Figure 13 presents the variation in the ^{235}U nuclide density of ES-FA with different BP candidates. The incorporation of the BP significantly affects the depletion rate of the fissile nuclide. PACS-L is capable of increasing the ^{235}U depletion speed. In contrast, the ES-FA with Lu_2O_3 retains the highest ^{235}U nuclide density.

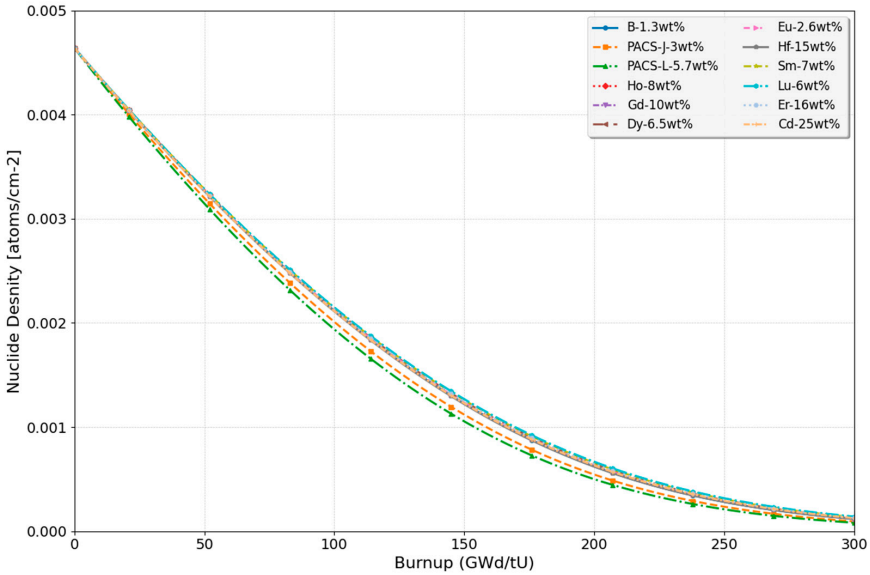


Figure 13. The burnup curves of the ^{235}U nuclide density of ES-FA with BP candidates.

3.3. Temperature Reactivity Feedback Coefficients

The negative temperature reactivity feedback is one of the important inherent control mechanisms of a nuclear reactor core. Unlike PWRs, which utilize a coolant density change to provide stable negative reactivity feedback, the epithermal-spectrum S–CO_2-cooled

reactor lacks this feature. Therefore, it is necessary to require that the addition of BP material assist in enhancing temperature feedback.

The fuel temperature coefficient (FTC) results for the FS-FA with BP candidates are summarized in Table 6. The BP weight fractions used in these calculations are consistent with those listed in Table 4. FTC values are computed over a temperature range of 890–910 K at each burnup step. These FS-FA results serve as a reference for subsequent comparisons with ES-FA. In Table 6, it is evident that most BPs decrease the magnitude of the FTC, except for PACS, where the hydrogen atoms have a thermalized neutron spectrum, thereby enhancing the neutron resonance absorption of ^{238}U.

Table 6. Summary of fuel temperature coefficients (pcm/K) for FS-FA containing different BP candidates at 0, 75, and 150 GWd/tU.

	Fuel Temperature Reactivity Coefficients (pcm/K)		
Poisonous Materials BP Mass Fraction	**0 GWd/tU**	**75 GWd/tU**	**150 GWd/tU**
Only UO_2 fuel assembly	−0.68	−0.74	−0.70
B_4C–2.3%	−0.34	−0.62	−0.56
Ho_2O_3–16%	−0.24	−0.2	−0.3
Eu_2O_3–7%	−0.14	−0.2	−0.26
Dy_2O_3–19%	−0.2	−0.12	−0.26
Gd_2O_3–19%	−0.36	−0.58	−0.28
HfO_2–27%	−0.66	−0.6	−0.5
Sm_2O_3–20%	−0.26	−0.36	−0.24
Er_2O_3–27%	−0.44	−0.42	−0.24
Lu_2O_3–13%	−0.26	−0.36	−0.2
PACS-J–3.3%	−1.56	−1.72	−1.90
CdO–31%	−0.46	−0.5	−0.56
PACS-L–5.4%	−1.84	−2.06	−2.14

Table 7 shows the FTC, moderator temperature coefficients (MTC), and total temperature coefficients (TTC) of ES-FA with BP candidates. The MTC temperature range is from 890 K to 910 K. The FTCs and MTCs are calculated from the isolated temperature oscillations of the fuel rods and ZrH2 moderator rods, while the TTCs are determined during simultaneous temperature changes. Apart from Er_2O_3, Eu_2O_3, and HfO_2, which demonstrate negative MTC at the BOL, the MTC of the remaining BP cases is slightly positive, suggesting these materials can effectively trigger negative temperature reactivity. Under an epithermal neutron spectrum, the increased proportion of resonance interactions amplifies the FTC magnitude. Among the BP candidates, the top four materials that maximize TTC are HfO_2, Er_2O_3, Gd_2O_3, and Eu_2O_3. The PACS material continuously shifts the neutron spectrum toward epithermal energies, resulting in higher temperature reactivity feedback.

Table 7. Summary of fuel, moderator, and total temperature coefficients (pcm/K) for ES-FA containing different BP candidates at 0, 50, and100 GWd/tU.

Poisonous Materials		**Temperature Reactivity Coefficients (pcm/K) 0**	**50 (GWd/tU)**	**100**	**Poisonous Materials**		**Temperature Reactivity Coefficients (pcm/K) 0**	**50 (GWd/tU)**	**100**
B_4C-1.3%	M	0	0.06	0.1	Eu_2O_3-2.6%	M	−0.08	0	0.06
	F	−1.5	−1.76	−1.94		F	−1.7	−1.54	−1.52
	T	−1.5	−1.7	−1.84		T	−1.78	−1.54	−1.46
PACS-J-3%	M	0	0.06	0.06	HfO_2-15%	M	−0.06	0.04	0.06
	F	−1.8	−2.1	−2.2		F	−2.1	−2	−1.96
	T	−1.8	−2.04	−2.1		T	−2.16	−1.96	−1.9
PACS-L-5.7%	M	0	0.06	0.06	Sm_2O_3-7%	M	0.14	0.12	0.1
	F	−2	−2.34	−2.46		F	−1.64	−1.6	−1.54
	T	−2	−2.28	−2.4		T	−1.5	−1.48	−1.44
Ho_2O_3-8%	M	0	0.06	0.06	Lu_2O_3-6%	M	0.06	0.14	0.1
	F	−1.5	−1.54	−1.64		F	−1.5	−1.46	−1.36
	T	−1.5	−1.48	−1.58		T	−1.44	−1.32	−1.26

Table 7. *Cont.*

Poisonous Materials		Temperature Reactivity Coefficients (pcm/K) 0	50 (GWd/tU)	100	Poisonous Materials		Temperature Reactivity Coefficients (pcm/K) 0	50 (GWd/tU)	100
Gd_2O_3-10%	M	0.1	0.14	0.14	Er_2O_3-16%	M	−0.22	0	0
	F	−1.88	−1.82	−1.78		F	−2.1	−1.86	−1.6
	T	−1.78	−1.68	−1.64		T	−2.32	−1.86	−1.6
Dy_2O_3-6.5%	M	0	0.06	0.08	CdO-25%	M	0	0.06	0.04
	F	−1.5	−1.52	−1.52		F	−1.7	−1.6	−1.44
	T	−1.5	−1.46	−1.44		T	−1.7	−1.54	−1.4

M: moderator temperature coefficients; F: fuel temperature coefficient; T: total temperature coefficients.

3.4. Flattening of Power Distribution

Achieving uniform power distribution in epithermal S–CO_2-cooled fuel assemblies is essential for improving safety. The evenness of power distribution can be measured by the assembly PPF, which is defined as the ratio of the maximum power density to the average power density of the fuel rods. Figure 14 shows the PPF values for FS-FA and ES-FA with BP candidates at the beginning, middle, and end of burnup stages. Excluding the effect of BP, the PPF values of ES-FA at three burnup stages are 1.0292, 1.0231, and 1.0184, respectively, compared to 1.0002, 1.0008, and 1.0025 for FS-FA.

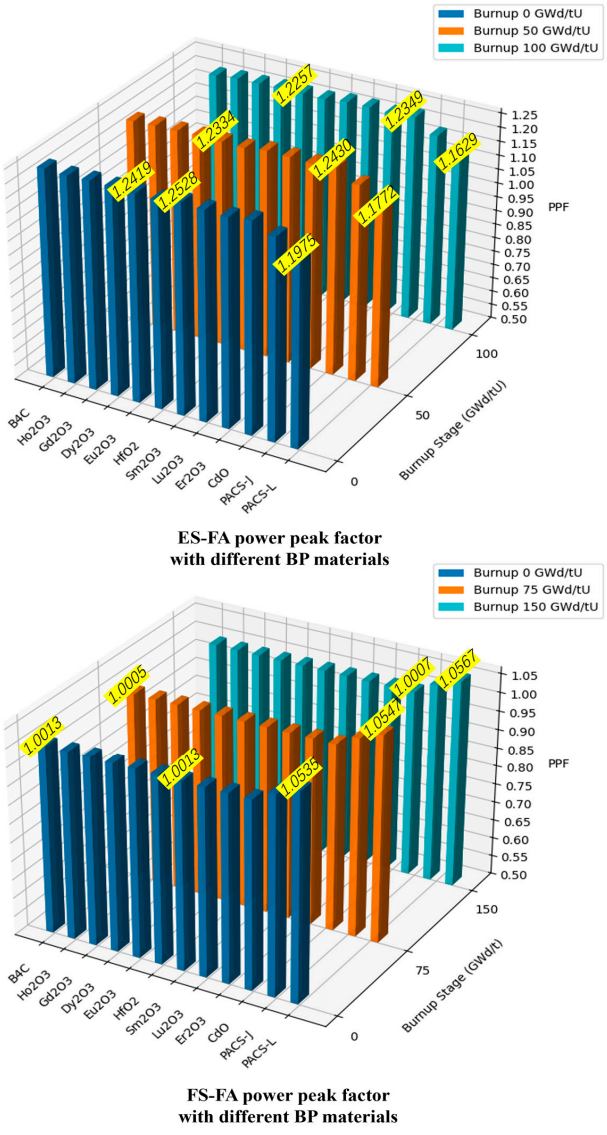


Figure 14. Power peaking factors at various burnup stages for FS-FA and ES-FA with different BP material candidates.

A clear finding from Figure 14 is that the PPFs in ES-FA are generally higher than those in FS-FA because moderator rods boost the fission rate in neighboring fuel rods. Compared to the Only UO_2 FS-FA, the PPFs of FS-FA containing BP materials other than PACS show only minor differences. At the BOL, the PPF of the Only UO_2 FS-FA is lower than that of cases with BP materials. However, by 150 GWd/tU, the PPF results are reversed. The candidate BPs tend to have small neutron absorption cross-sections in the fast neutron energy range, leading to a limited effect on power distribution. Other factors influencing PPF include the fuel content and adjustments in fuel ND, which are discussed in Section 3.1.4. These factors can cause uneven distributions of fissile ^{235}U, resulting in high PPF values at the BOL.

Among these rare-earth element poisons, ES-FA's PPF with HfO_2 consistently remains lower than others, indicating its ability to sustain effective power distribution control throughout the burnup process. For ES-FA containing B_4C, the PPFs are generally lower than those of other compound materials, although they are relatively higher at BOL. This behavior results from the strong neutron absorption capability and rapid depletion rate of B_4C. As a result, its influence on the PPF becomes negligible at burnups of 50 and 100 GWd/tU. The ES-FA, which contains PACS and exhibits both neutron moderation and absorption capabilities, continues to demonstrate lower PPFs compared to other assemblies, highlighting excellent performance. Among ES-FA, the BPs that effectively reduce the PPF are PACS, HfO_2, and Eu_2O_3.

3.5. BP Performance Assessment

Reactivity suppression, temperature reactivity feedback, burnup behavior, and power distribution flattening have been evaluated. Based on the results, a comprehensive BP material selection can be made.

Eu_2O_3 exhibited outstanding performance as BP in epithermal S–CO_2-cooled reactors. With a low mass fraction of 2.6%, Eu_2O_3 achieved effective reactivity suppression while maintaining a stable total temperature coefficient (TTC below -1.4 pcm/K) and ensuring flat power distributions (PPF ≤ 1.24) throughout the burnup process.

HfO_2 demonstrated distinct advantages for long-term BP applications. At a higher mass fraction (~15%), HfO_2 not only provided stronger suppression of reactivity and improved temperature reactivity feedback (TTC < -2 pcm/K) but also produced neutron absorption products that maintained spectral adaptability, ensuring effective reactivity control up to 93 GWd/tU. This characteristic makes HfO_2 an ideal candidate for long-term reactor operation. In addition, Er_2O_3 was particularly effective in enhancing temperature feedback, showing the most negative TTC (-2.32 pcm/K initially) among rare-earth BPs.

The innovative PACS materials addressed trade-offs between moderation and absorption by utilizing hydrogen's spectral softening and boron's capture capabilities. PACS-L is especially well balanced for high burnup (>105 GWd/tU) and TTC (-2 pcm/K), offering a pathway for next-generation BP material development.

As mentioned in Section 3.1.1, this study reassesses the k_{inf} and TTC at BOL of the design cases with Eu_2O_3, HfO_2, Er_2O_3, and PACS-J candidates using OpenMC. A comparison of the results from KYLIN-I and OpenMC is presented in Table 8. The OpenMC simulation settings are consistent with those used in Figure 4 ES-FA benchmark.

Since KYLIN-I employs a 45-group multi-group while OpenMC uses a continuous energy cross-section library, the initial k_{inf} values obtained with KYLIN-I are systematically higher than those from OpenMC by 400–500 pcm, stable with the benchmark results. In addition, OpenMC adopts a 300 K temperature gap to calculate the TTC, resulting in values that are generally more negative than those from KYLIN-I. Nevertheless, this discrepancy does not alter the relative performance of BP in enhancing the reactivity feedback of the

ES-FA. The above comparison demonstrates that the code's sensitivity does not affect the evaluation and selection of BPs. The ranking and selection of BP in this study guides engineering design of epithermal-spectrum S–CO_2-cooled reactors.

Table 8. Comparison of k_{inf} and TTC at BOL with KYLIN-I and OpenMC.

	KYLIN-I		OpenMC	
	Initial k_{inf}	**TTC (pcm/K)**	**Initial k_{inf}**	**TTC (pcm/K)**
Eu_2O_3-2.6%	1.20391	−1.78	1.19942 ± 0.00007	−1.96
HfO_2-15%	1.20305	−2.16	1.19893 ± 0.00007	−2.42
Er_2O_3-16%	1.19960	−2.32	1.19466 ± 0.00007	−2.49
PACS-L-5.7%	1.19988	−1.80	1.19550 ± 0.00007	−2.04

4. Conclusions

The findings from this study confirm that aligning the neutron spectrum is a crucial principle for selecting BPs in an epithermal-spectrum S–CO_2-cooled reactor. The specific neutron cross-section characteristics and isotope transmutation pathways of different materials determine their performance rankings. The Eu_2O_3, HfO_2, Er_2O_3, and PACS four materials are selected as suitable epithermal-spectrum reactor BP materials.

It should be noted that, even though the neutron spectrum is thermalized by ZrH_2 moderator rods, the required weight fractions for HfO_2 and Er_2O_3 are around 15%. Such high weight fractions can adversely affect the thermal conductivity and manufacturability. Therefore, future work will focus on optimizing the assembly configuration. For example, the next study will adjust the positions of the moderator and BP rods. The selection of BP materials is based on the intrinsic neutronic merits of Eu_2O_3, HfO_2, Er_2O_3, and PACS. The goal is to reduce the required BP weight fractions while enhancing the effectiveness of reactivity control. Meanwhile, in the practical engineering design, materials may be selected or combined based on the reactor's anticipated operational period and power density to achieve strong reactivity suppression at the BOL and sustained control throughout the lifetime of an epithermal S–CO_2-cooled reactor.

Author Contributions: Conceptualization, W.W., Y.Z. and N.J.; methodology, Y.Z., D.L. and L.W.; validation, J.W.; formal analysis, B.Z., W.W. and D.L.; writing—original draft preparation, Y.Z.; visualization, J.W.; investigation, X.Z. All authors have read and agreed to the published version of the manuscript.

Funding: This research received no external funding.

Data Availability Statement: The data that support the findings of this study are available from the corresponding author upon reasonable request.

Conflicts of Interest: The authors declare no conflicts of interest.

Abbreviations

The following abbreviations are used in this manuscript:

BP	Burnable Poison
S-CO_2	Supercritical Carbon Dioxide
TTC	Total Temperature Coefficient
FTC	Fuel Temperature Coefficient
MTC	Moderator Temperature Coefficient
AGR	Advanced Gas-Cooled Reactor
HTGR	High-Temperature Gas-Cooled Pebble-Bed Reactor
HTTR	High-Temperature Engineering Test Reactor

MIT	Massachusetts Institute of Technology
SNL	Sandia National Laboratories
SMR	Small Modular Reactor
LMCR	Liquid Metal-Cooled Fast Spectrum Reactor
PACS	Polycarborane-Siloxane-Ethynyl Polymer
ES-FA	Epithermal-Spectrum Fuel Assembly
FS-FA	Fast-Spectrum Fuel Assembly
MCM	Monte Carlo Method
PC	Predictor–Corrector

References

1. Zhang, Z.; Dong, Y.; Li, F.; Zhang, Z.; Wang, H.; Huang, X.; Li, H.; Liu, B.; Wu, X.; Wang, H.; et al. The Shandong Shidao Bay 200 MWe High-Temperature Gas-Cooled Reactor Pebble-Bed Module (HTR-PM) Demonstration Power Plant: An Engineering and Technological Innovation. *Engineering* **2016**, *2*, 112–118. [CrossRef]
2. Nagatsuka, K.; Noguchi, H.; Nagasumi, S.; Nomoto, Y.; Shimizu, A.; Sato, H.; Nishihara, T.; Sakaba, N. Current status of high temperature gas-cooled reactor development in Japan. *Nucl. Eng. Des.* **2024**, *425*, 113338. [CrossRef]
3. IAEA. *High Temperature Gas Cooled Reactor Fuels and Materials*; International Atomic Energy Agency: Vienna, Austria, 2010.
4. Liu, Y.; Wang, Y.; Huang, D. Supercritical CO_2 Brayton cycle: A state-of-the-art review. *Energy* **2019**, *189*, 115900. [CrossRef]
5. Teja, D.V.H.; Muvvala, P.; Prashanth Nittala, N.A.; Bandhu, D.; Khan, M.I.; Saxena, K.K.; Khan, M.I. Comparative performance analysis of recuperative helium and supercritical CO_2 Brayton cycles for high-temperature energy systems. *Energy* **2024**, *312*, 133469. [CrossRef]
6. Wu, P.; Ma, Y.; Gao, C.; Liu, W.; Shan, J.; Huang, Y.; Wang, J.; Zhang, D.; Ran, X. A review of research and development of supercritical carbon dioxide Brayton cycle technology in nuclear engineering applications. *Nucl. Eng. Des.* **2020**, *368*, 110767. [CrossRef]
7. Handwerk, C.S.; Driscoll, M.J.; Hejzlar, P. Optimized Core Design of a Supercritical Carbon Dioxide-Cooled Fast Reactor. *Nucl. Technol.* **2008**, *164*, 320–336. [CrossRef]
8. Pope, M.A. *Reactor Physics Design of Supercritical CO_2-Cooled Fast Reactors*; Massachusetts Institute of Technology: Cambridge, MA, USA, 2004.
9. Vaclav, D. A Supercritical Carbon Dioxide Cycle for Next Generation Nuclear Reactors. Ph.D. Thesis, Massachusetts Institute of Technology, Cambridge, MA, USA, 2004.
10. Moisseytsev, A.; Sienicki, J.J. Investigation of alternative layouts for the supercritical carbon dioxide Brayton cycle for a sodium-cooled fast reactor. *Nucl. Eng. Des.* **2009**, *239*, 1362–1371. [CrossRef]
11. Yu, H.; Hartanto, D.; Oh, B.S.; Lee, J.I.; Kim, Y. Neutronics and Transient Analyses of a Supercritical CO_2-cooled Micro Modular Reactor (MMR). *Energy Procedia* **2017**, *131*, 21–28. [CrossRef]
12. Zhang, Y.; Peng, M.; Xia, G.; Lv, L. Transient thermal–hydraulic analysis of SCO_2-cooled reactor system with modified RELAP5. *Ann. Nucl. Energy* **2020**, *147*, 107681. [CrossRef]
13. Niu, Y.; Sun, D.; Zhang, Y.; Chen, L.; Peng, M.; Xia, G. Operation characteristics analysis of supercritical CO_2 reactor based on neutronics and thermal-hydraulics coupling. *Nucl. Eng. Des.* **2025**, *436*, 113947. [CrossRef]
14. Zhang, F.; Zhu, G.; Zou, Y.; Yan, R.; Xu, H. Conceptual design and neutronic analysis of a megawatt-level vehicular microreactor based on TRISO fuel particles and S-CO_2 direct power generation. *Nucl. Sci. Tech.* **2022**, *33*, 69. [CrossRef]
15. Zhang, F.; Zhu, G.; Zou, Y.; Yan, R.; Xu, H. Core nuclear design and heat transfer analysis of a megawatt-level SiC coated particle based vehicular micro reactor. *Nucl. Eng. Des.* **2023**, *415*, 112668. [CrossRef]
16. Lu, D.; Wang, L.; Cai, Y.; Wang, D.; Zhang, C. Physical Design of High-Performance Fuel Assembly Based on Fully Ceramic Microencapsulated Fuel for Supercritical CO_2 Cooled Reactor. *Front. Energy Res.* **2021**, *9*, 764905. [CrossRef]
17. Wang, L.; Lu, D.; Yao, L.; Xiang, H.; Zhao, C. Study on Temperature Feedback Effect of Supercritical CO_2–Cooled Reactor. *Front. Energy Res.* **2021**, *9*, 764906. [CrossRef]
18. Choi, H.Y.; Park, C.J. Conceptual design of thorium based epithermal spectrum reactor. *Ann. Nucl. Energy* **2017**, *109*, 61–68. [CrossRef]
19. Evans, J.A.; DeHart, M.D.; Weaver, K.D.; Keiser, D.D. Burnable absorbers in nuclear reactors—A review. *Nucl. Eng. Des.* **2022**, *391*, 111726. [CrossRef]
20. Grossbeck, M.; Renier, J.P.A. *Development of Improved Burnable Poisons for Commercial Nuclear Power Reactors*; Oak Ridge National Lab. (ORNL): Oak Ridge, TN, USA, 2002.
21. Zhou, S.; Shi, X. Reactor Reactivity and Feedback Mechanism Research. *Nucl. Electron. Detect. Technol.* **2013**, *33*, 955–959.

22. Dandi, A.; Kim, M.H. Conceptual design of the double tube burnable poison for the next generation small modular reactor. *Ann. Nucl. Energy* **2023**, *186*, 109776. [CrossRef]
23. Min, G.; Shen, X.; Xue, J.; Wang, L.; Jiang, N. Data-fusion-based variable-fidelity reduced-order model for accurate thermal–hydraulic behavior prediction in a 6 × 6 rod bundle. *Ann. Nucl. Energy* **2026**, *226*, 111905. [CrossRef]
24. Tiang, Z.H.; Xiao, S.C. Long-term reactivity control of accident tolerant fuel loaded marine small modular reactor using particle-type burnable poisons. *Ann. Nucl. Energy* **2021**, *156*, 108177. [CrossRef]
25. Xu, S.; Yu, T.; Xie, J.; Li, Z.; Xia, Y.; Yao, L. Selection of burnable poison in plate fuel assembly for small modular marine reactors. *Nucl. Eng. Technol.* **2022**, *54*, 1526–1533. [CrossRef]
26. Guo, H.; Sciora, P.; Kooyman, T.; Buiron, L.; Rimpault, G. Application of Boron Carbide as Burnable Poison in Sodium Fast Reactors. *Nucl. Technol.* **2019**, *205*, 1433–1446. [CrossRef]
27. Wu, Y.; Shen, Y.; Jin, X.; Song, Q.; Xiao, Y.; Guo, H.; Gu, H. Development of a design method for burnable poisons in small modular fast reactors. *Ann. Nucl. Energy* **2025**, *211*, 111008. [CrossRef]
28. Obara, T.; Onoe, T. Flattening of burnup reactivity in long-life prismatic HTGR by particle type burnable poisons. *Ann. Nucl. Energy* **2013**, *57*, 216–220. [CrossRef]
29. Simanullang, I.L.; Fujimoto, N. Study on potential burnable poison materials for a small modular block-type HTGR design using MgO-BeO as a composite-based moderators. *Nucl. Eng. Des.* **2025**, *431*, 113742. [CrossRef]
30. Chai, X.; Liu, X.; Guan, C.; Zhang, T.; Liu, X. Investigation of reactivity control strategies for a micro-transportable gas-cooled thermal reactor. *Nucl. Eng. Des.* **2024**, *416*, 112758. [CrossRef]
31. Zhang, C.; Yuan, Y.; Du, S.; Liu, G.; He, K.; Yang, H.; Huo, X. Research on burnable poison in micro gas-cooled reactor. *High Power Laser Part. Beams* **2022**, *34*, 026010.
32. Yu, H.; Hartanto, D.; Moon, J.; Kim, Y. A Conceptual Study of a Supercritical CO_2-Cooled Micro Modular Reactor. *Energies* **2015**, *8*, 13938–13952. [CrossRef]
33. Zhang, Y.; Li, R.; Zhang, B.; Miao, Y.; Guo, C.; Xia, G.; Peng, M. Design and performance analysis of 15MWth SCO_2-cooled micro reactor. *Nucl. Eng. Technol.* **2025**, *57*, 103863. [CrossRef]
34. Yi, Z.; Kun, Z.; Di, L.; Shengdong, Q. Study on Reactivity Disturbance Characteristics of SCO_2 Reactor Assembly Caused by Burnable Poisons. *Nucl. Power Eng.* **2023**, *44*, 153–159.
35. Ikeda, K.; Moriwaki, H.; Ohkubo, Y.; Iwasaki, T.; Konashi, K. Application of hafnium hydride control rod to large sodium cooled fast breeder reactor. *Nucl. Eng. Des.* **2014**, *278*, 97–107. [CrossRef]
36. Galahom, A.A. Study of the possibility of using Europium and Pyrex alloy as burnable absorber in PWR. *Ann. Nucl. Energy* **2017**, *110*, 1127–1133. [CrossRef]
37. Kang, Y.R.; Lee, M.W.; Ro, T.I.; Kim, G.N.; Danon, Y.; Williams, D. Neutron Capture Measurements and Resonance Analysis of Dysprosium. *Nucl. Data Sheets* **2014**, *119*, 162–164. [CrossRef]
38. Youinou, G.J.; Palmiotti, G.; Salvatores, M.; Nimmagadda, J.K.; Imel, G.; Giglio, J.; Giglio, T.; Berg, J.; Sterbentz, J.; Nielsen, J.; et al. Measurements of effective actinides neutron capture cross sections in a cadmium-filtered epithermal neutron spectrum. *Ann. Nucl. Energy* **2021**, *159*, 108348. [CrossRef]
39. Mustafa, S.S. Neutronic investigation of enriched gadolinium, natural gadolinium and Zirconium-erbium as burnable poisons in the advanced PWR assemblies by MCNPX code. *Radiat. Phys. Chem.* **2023**, *212*, 111129. [CrossRef]
40. Moreira, O. Analysis of 149Sm time evolution and the reactivity contribution in nuclear reactors. *Ann. Nucl. Energy* **2015**, *83*, 87–93. [CrossRef]
41. Luo, J.; Tuo, F.; Kong, X. Measurements of activation cross sections for 175Lu(n,α)172Tm, 176Lu(n,α)173Tm and 175Lu(n,p)175m+gYb reactions induced by neutrons around 14MeV. *Ann. Nucl. Energy* **2011**, *38*, 1693–1697. [CrossRef]
42. Smith, A.B. Fast-neutrons incident on holmium. *Ann. Nucl. Energy* **2001**, *28*, 1745–1758. [CrossRef]
43. Khoshahval, F. Performance analysis of an advanced polymeric burnable poison for PWR fuel assembly. *Eur. Phys. J. Plus* **2024**, *139*, 73. [CrossRef]
44. Chang, Q.; Guo, S.; Zhang, X. Radiation shielding polymer composites: Ray-interaction mechanism, structural design, manufacture and biomedical applications. *Mater. Design* **2023**, *233*, 112253. [CrossRef]
45. More, C.V.; Alsayed, Z.; Badawi, M.S.; Thabet, A.A.; Pawar, P.P. Polymeric composite materials for radiation shielding: A review. *Environ. Chem. Lett.* **2021**, *19*, 2057–2090. [CrossRef]
46. Li, J.; She, D.; Shi, L. An improved reactivity-equivalent physical transformation for treating FCM fuel with burnable poisons. *Ann. Nucl. Energy* **2018**, *121*, 577–581. [CrossRef]
47. Hongbo, Z.; Xingjie, P.; Chen, Z.; Wenbo, Z.; Zhang, C.; Qing, L.; Yingrui, Y.; Zhaohu, G. Subgroup method for the high fidelity neutronics code SHARK and preliminary benchmarking. *Nucl. Eng. Des.* **2023**, *408*, 112308. [CrossRef]
48. He, Q.; Yi, S.; Liu, Z.; Wu, H.; Cao, L. A one-dimensional model for multi-group equivalence parameters in subgroup method. *Ann. Nucl. Energy* **2022**, *175*, 109208. [CrossRef]

49. Stimpson, S.; Liu, Y.; Collins, B.; Clarno, K. A lumped parameter method of characteristics approach and multigroup kernels applied to the subgroup self-shielding calculation in MPACT. *Nucl. Eng. Technol.* **2017**, *49*, 1240–1249. [CrossRef]
50. Chen, Z.; Zhang, Z.; Ju, H.; Yao, D.; Huang, S.; Ni, D. Benchmark Verification of Fuel Assembly Few Group Parameter Calculation Code KYLIN-1. *Hedongli Gongcheng/Nucl. Power Eng.* **2017**, *38*, 11–14.
51. Romano, P.K.; Horelik, N.E.; Herman, B.R.; Nelson, A.G.; Forget, B.; Smith, K. OpenMC: A state-of-the-art Monte Carlo code for research and development. *Ann. Nucl. Energy* **2015**, *82*, 90–97. [CrossRef]
52. Wang, B.; Zhao, W.; Zhang, H.; Zhao, C.; Chen, Z.; Liu, K.; Gong, Z.; Zeng, W.; Li, Q. Validation of whole core transport code SHARK with HPR1000 experiment. *Ann. Nucl. Energy* **2024**, *199*, 110337. [CrossRef]

Disclaimer/Publisher's Note: The statements, opinions and data contained in all publications are solely those of the individual author(s) and contributor(s) and not of MDPI and/or the editor(s). MDPI and/or the editor(s) disclaim responsibility for any injury to people or property resulting from any ideas, methods, instructions or products referred to in the content.